Yielding and crystallization of colloidal gels under oscillatory shear

P. A. Smith,[1] G. Petekidis,[2,*] S. U. Egelhaaf,[1,3] and W. C. K. Poon[1,†]
[1]*SUPA, School of Physics, The University of Edinburgh, Mayfield Road, Edinburgh EH9 3JZ, United Kingdom*
[2]*IESL-FORTH and Department of Materials Science and Technology, University of Crete, Heraklion, 71110 Crete, Greece*
[3]*Condensed Matter Physics Laboratory, Heinrich-Heine-University, D-40225 Düsseldorf, Germany*
(Received 1 July 2007; published 15 October 2007)

We have studied the behavior of a colloidal gel under oscillatory shear. The quiescent gel was an arrested structure formed by a 40% volume fraction hard-sphere suspension in which a "depletion" interparticle attraction was induced by adding nonadsorbing polymer. We applied progressively larger amplitude oscillatory shear to the sample, and observed its behavior using conventional and confocal microscopy as well as dynamic light scattering echo spectroscopy. We find that, to within experimental uncertainties, the point at which irreversible particle rearrangements (or yielding) occur coincides with the observation of crystallization. We summarize our findings in a "shear state diagram." The strain amplitude required for yielding/crystallization increases with decreasing oscillation frequency. We can quantitatively account for our observations by estimating the effect of shear on the probability for a particle to escape from the attractive potential of its neighbor using a Kramers approach.

DOI: 10.1103/PhysRevE.76.041402 PACS number(s): 82.70.Dd, 83.60.Rs, 83.80.Hj

I. INTRODUCTION

Under suitable conditions, colloidal suspensions can form "soft solids"—materials with finite yield stress in the (say) $10^{-3}-10^{3}$ Pa range. In uncharged systems, or systems in which the charges are substantially screened out by salt, both amorphous (glassy) and ordered (crystalline) states are known at high particle volume fractions. At low volume fractions, (amorphous) gel states can be formed. To study these soft colloidal solids is interesting for both fundamental and applied reasons. Fundamentally, understanding the static and dynamic properties of these solidlike states in their own right poses a significant challenge to statistical mechanics. Moreover, they can function as experimental models for certain generic phenomena in condensed matter physics, such as melting [1] and the glass transition [2]. Practically, soft colloidal solids occur ubiquitously in industrial processes and products, and may form the basis of future applications, such as photonic crystals. The study of model colloidal solids has recently received a boost due to the availability of confocal microscopy. Using this technique on suspensions of fluorescently-labeled particles yields real-time, real-space information at the single-particle level [3–5].

A major concern in the fundamental and applied research on soft colloidal solids is to understand their deformation, yielding and flow under externally applied stresses, in other words, their linear and nonlinear rheology. The rheology of polymers has been well understood for at least a decade: their bulk properties can now be related quantitatively to molecular details [6]. In comparison, the understanding of the rheology of concentrated colloidal suspensions lags significantly behind. This is partly because, compared to polymers, even modest shear can significantly perturb the local equilibrium of a suspension. Moreover, the small number of nearest neighbors in a colloid (always $\lesssim 10$) renders a mean-field approach inapplicable; this contrasts strikingly with polymers, where the many chains (usually $\gtrsim 10^{3}$) constraining any individual macromolecule can be well modeled by a mean-field "tube."

There have been some recent advances in the understanding of the rheology of colloidal solids. On the theory front, mode coupling theory (MCT), which can give a good quantitative account of the properties of colloidal glasses [7], has been extended to deal with steady and time-dependent shear [8,9]. Hopping processes, which do not feature in MCT proper, can also be included and their effect on rheology studied [10]. On the experimental front, confocal microscopy has been used to give an account of the deformation and flow of a confined colloidal crystal to an unprecedented level of detail; the information obtained then suggested a simple heuristic theory [4]. The shear cells available for such experiments are also becoming increasingly sophisticated [5,11]. One advantage of microscopy, confocal as well as conventional, in such studies is its ability to obtain *local* information. This is vital, since it is increasingly realized that the bulk rheology of many soft materials (including colloidal solids) may be dominated by inhomogeneities in their microstructure and the associated local processes, so that methods that average over time and/or space may miss vital aspects. On the other hand, dynamic light scattering under oscillatory shear (LS echo) [11–13] provides invaluable information on the microscopic particle dynamics over a wide range of relaxation times, which is averaged over a huge ensemble and thus in general provides excellent statistics.

In this work, we study the deformation and yielding of a well-characterized, model soft colloidal solid—a relatively dense gel formed in a system of hard-sphere colloids (volume fraction $\phi \approx 0.4$) with a short-range attraction induced by nonadsorbing polymers. Adding a nonadsorbing polymer to a hard-sphere suspension induces an attraction between the particles by a "depletion effect." Exclusion of polymer from the region between the surfaces of two nearby colloids creates an unbalanced osmotic pressure pushing the particles

*georgp@iesl.forth.gr
†w.poon@ed.ac.uk

TABLE I. Properties of the samples used in this study. Sample A was used in conventional microscopy and echo light scattering (Sec. III A), while sample B was used in confocal microscopy (Sec. III B). Abbreviations: "*cis*-D" indicates *cis*-decalin and "$\Delta\rho=0$" is a density-matching mixture of *cis*-decalin and cycloheptyl bromide. ϕ is the volume fraction of colloid, c_p/c^* is the concentration of the polymer in units of the overlap concentration c^*, R is the colloid radius, r_g is the polymer radius of gyration, $\xi=r_g/R$ is their ratio at low polymer concentrations, and $\xi^*=r_g^*/R$ the ratio between mesh size and colloid size applicable at high polymer concentrations. U_{dep}/k_BT is the depth of the depletion attraction at contact in units of the thermal energy k_BT.

	Solvent	ϕ	c_p/c^*	R (nm)	r_g (nm)	ξ	ξ^*	U_{dep}/k_BT
A	*cis*-D	0.40	1.5±0.1	689	108	0.156	0.052	−22±8
B	$\Delta\rho=0$	0.44	1.6±0.1	1122	113	0.101	0.028	−46±16

together. The resulting effective pair attraction can be modeled, at least at low ϕ, by a potential of the Asakura-Oosawa form [14]. Its range is given by the size of the polymer coils as measured by twice the coil's radius of gyration r_g. It is convenient to measure this range in units of the hard-sphere radius, R, i.e., by the size ratio $\xi=r_g/R$. The depth of the depletion attraction U_{dep} is proportional to the concentration of polymers in the free volume left to them by the colloids. (U_{dep} denotes the attractive potential at contact, i.e. $U_{\mathrm{dep}}<0$).

A convenient experimental realization of such a colloid-polymer mixture consists of suspensions of sterically stabilized poly-(methylmethacrylate) (PMMA) particles suspended in various simple hydrocarbon liquids (most popularly, decalin) with added linear polystyrene (PS). The equilibrium phase behavior of this system as well as the quiescent properties of various high- and low-ϕ arrested states have been well studied [15–17]. In particular, at high enough polymer concentrations, the system forms arrested states dominated by the interparticle attraction: glasses and gels at high and low ϕ, respectively. Whether there are any fundamental differences between attraction-dominated glasses and gels other than particle density is an open question.

Estimating the range and depth of the depletion potential between particles in such concentrated systems is problematic. First, the usual expression used to estimate the volume available to the polymers from scaled particle theory [18] has been found to be significantly inaccurate at high ϕ [19]. Nevertheless, we continue to use this expression, since no others are available. Second, as the polymer concentration increases beyond the overlap concentration c^*, the range of the depletion potential ceases to be controlled by r_g, but instead scales as the correlation length (or mesh size) r_g^*, which shrinks with concentration above c^*. The relevant size ratio then is defined as $\xi^*=r_g^*/R$. Third, at these concentrations, the osmotic pressure of the polymer is grossly nonideal. The effects of shrinking correlation length and nonideal osmotic pressure, together with the curvature of the particle surfaces, are considered in a "modular" fashion by Aarts and Lekkerkerker [20]. We use this approach and the scaled particle theory expression for the free volume to estimate the range and depth of the depletion potential in what follows.

Here we study gels in a mixture of PMMA colloids and PS polymers at $\phi\approx 0.4$. We show that under oscillatory shear of increasing amplitude, the gel yields and crystallizes. We demonstrate that the process can be followed in great detail using optical microscopy (both conventional and confocal) and LS echo measurements. As in a previous study of a hard-sphere colloidal glass made up of the same particles [21], we find that, to within experimental uncertainties, the point at which irreversible particle rearrangements (or yielding) occur coincides with the observation of crystallization. We discuss this finding in the light of recently discovered differences in the yielding behavior of systems in which arrest is driven by repulsion and attraction, respectively [22]. An informative way to summarize our data is in the form of a shear state diagram which shows under what conditions a gel undergoing oscillatory shear will yield and crystallize. We propose a simple model that can account for the observed yielding or crystallization boundary on the shear state diagram.

II. MATERIALS AND METHODS

A. Samples

We used PMMA colloids (synthesized in-house) suspended in either *cis*-decalin or *cis*-decalin with enough cycloheptyl bromide (CHB) added to match the density of the particles (as evidenced by prolonged centrifugation). PS of molecular weight $M_w=7.3\times 10^6$ g/mol was used as purchased from Polymer Laboratories. The properties of the two samples investigated in this work are shown in Table I. Sample A was used in conventional microscopy and light scattering. Sample B was used for confocal microscopy; the larger particles enabled more accurate determination of their positions.

Particle radii were determined from the lattice spacing of colloidal crystals coexisting with colloidal fluid assuming that the former has $\phi=0.545$. We did not measure the polydispersity; however, the observation of crystals implies that the polydispersity is less than about 10%. The value of the particle radius reported for sample B takes into account an about 2% swelling, which is caused by the addition of CHB [23]. Colloid stock was prepared by redispersing spun-down sediments (assumed to be at $\phi=0.64$) and with enough solvent added to give the desired final volume fraction. In the case of sample B, density matching was defined to be at no visible sedimentation after centrifuging for 24 h; nevertheless, a few days of centrifugation did eventually give rise to sedimentation, which enables the preparation of a stock solution using the method described above.

The radius of gyration, r_g, of PS in sample A was estimated using data for PS *in cis*-decalin [24]. CHB swells PS;

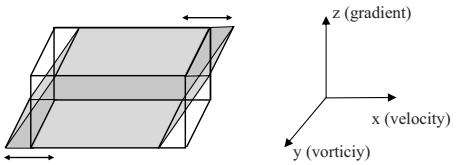

FIG. 1. Schematic diagram illustrating the applied shear strain and our axes convention.

we estimate r_g in sample B using literature data [25]. We estimate the overlap concentration c^* at which the coil volume fraction reaches about 1 by taking the coil volume to be $(4/3)\pi r_g^3$. Then, using the approach of [20] and the free volume expression [18], we estimate the depth and range of the polymer-induced depletion potential. The large uncertainty in each value reflects the way errors propagate from uncertainties in R and r_g. Moreover, the relations used [20] assume that the polymer is in an athermal solvent; since we do not expect PS to be fully swollen *in cis*-decalin with or without CHB, the values quoted should be treated as upper bounds.

To prepare for observations, we first tumble a sample to ensure homogenization. Then small portions were withdrawn and loaded into a variety of shear cells for microscopy or light scattering [26]. (Figure 1 shows our shear geometry and illustrates our axes convention.) The gel latency time in the case of the non-density-matched sample was determined by direct observation to be about 50 h. All observations using sample A were obtained within a few hours of loading a freshly homogenized sample and therefore well within the window of stability indicated by this latency time.

B. Conventional and confocal microscopy

Conventional microscopy was performed using a Zeiss Axioscope FS. Images were taken with a 100× oil immersion differential interference contrast (DIC) objective with a working distance of 0.15 mm. Additional magnification was provided by a 1.25× or 1.6× lens in front of the camera. DIC was used to enhance the poor contrast found in colloidal samples [27]. Images of the sample were obtained by digitizing frames via a computer-controlled charge-coupled device (CCD) camera.

Confocal microscopy was conducted using a Nikon Eclipse TE300 microscope fitted with a Biorad Radiance 2100 scanning system together with an argon ion laser operating at a wavelength $\lambda=488$ nm and an output power of 0.05 W. Emission from the fluorescent particles was detected for $\lambda>500$ nm. The 100× and 60× Nikon oil immersion objectives had working distances of 0.13 and 0.21 mm, respectively.

The parallel-plate shear cells used for microscopy [26] were similar to the one for light scattering described before [11,12]. A putative zero-shear plane exists where the particles are stationary. However, blurring from particles above and below this plane rendered imaging of the stationary plane impossible during shear. Consequently, shear was stopped periodically to allow for images to be recorded. The strain was applied for equal intervals, typically 2 min. A plate separation of 0.3 mm is used in all microscopy experiments. The degree of turbidity of our samples permitted usable images to be obtained to about 100 μm into the sample.

The output from confocal microscopy consisted of stacks of images obtained by scanning successive depths within a sample. It took typically about 3 min to record 100 image slices from a volume of about $50\times50\times20\mu$m, which typically contained some 30 000 particles. The coordinates of these particles were subsequently reconstructed from each image stack using established methods [28] which have been extended and kindly provided to us by Professor Eric Weeks.

C. Light scattering echo

We investigate particle motion by dynamic light scattering under multiple scattering conditions. The dynamic light scattering echo technique (LS echo) [12,13,29] monitors particle rearrangements in a sample under oscillatory shear by measuring the intermediate scattering function. The time dependence of the scattered intensity of a single speckle, $I(t)$, is measured and the normalized time autocorrelation function of the scattered intensity $g^{(2)}(\tau)=\langle I(\tau+t)I(t)\rangle/\langle I(t)\rangle^2$ calculated under multiple scattering conditions in the transmission geometry. The resulting $g^{(2)}(\tau)$ exhibits "echoes" at delay times equal to multiples of the oscillation period T. The trivial contribution of the shear induced affine motion can be excluded by following the peaks of the echoes. Thus, any reduction in the amplitude of the echoes, $g^{(2)}(\tau_m=mT)$ with $m=1,2,3,\ldots$, provides a measure of the degree of the irreversible rearrangement due to Brownian motion and shear. As discussed elsewhere [12], for multiply scattering samples we may write

$$g^{(1)}(\tau_m)=\sqrt{g^{(2)}(\tau_m)-1}\simeq\exp\left\{\frac{-Nk^2}{6}[\langle\Delta r^2(\tau_m)\rangle_B+\langle\Delta r^2(\tau_m)\rangle_S]\right\},$$

where $k=2\pi/\lambda$, N is the average number of times a photon is scattered between entering and leaving the sample, while $\langle\Delta r^2(\tau_m)\rangle_B$ is the mean-square displacement associated with Brownian motion and $\langle\Delta r^2(\tau_m)\rangle_S$ is that caused by shear. The length scale being probed, l_{DWS}, is controlled by experimental conditions. If the samples scatter strongly the length scale probed is $l_{\mathrm{DWS}}=\sqrt{6}/\sqrt{Nk}$. As in our previous work on the yielding of hard-sphere glasses [12], here we work with transmitted light that has been (on average) scattered twice [30], thus probing motions on a length scale of about $R/4$.

The parallel-plate shear cell used for light scattering has been described before [11,12]. The sample is illuminated from below by a helium-neon laser ($\lambda=633$ nm) with 20 mW output power and the scattered light is detected in transmission geometry by a single-mode fiber connected to an avalanche photodiode operating in the photon counting mode. A crossed polarizer before the fiber removes any residual (polarized) single scattering. The signal is processed by a linear correlator (Flex410R, Correlator.com), which allows the clustering of delay channels around specific delay times. This feature permits an accurate measurement of narrow echoes.

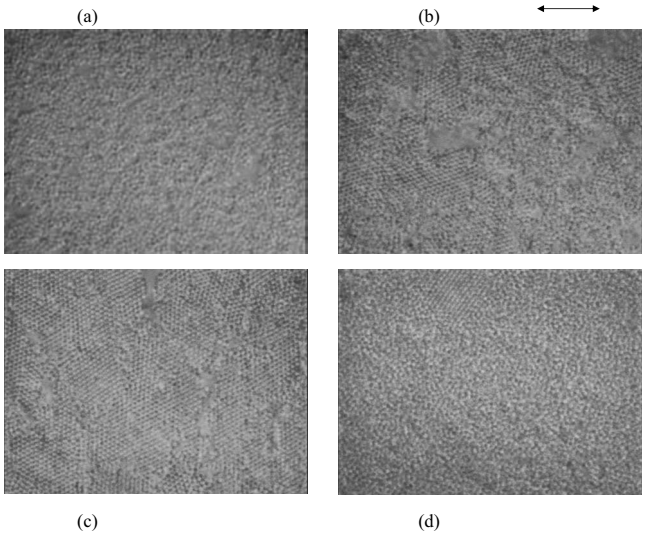

FIG. 2. Optical DIC microscopy images of a colloid-polymer gel in the quiescent state (a), after 2 min of oscillatory shear at a frequency of $f=70$ Hz and a strain amplitude of $\gamma_0=0.13$ (b), 0.27 (c), and 0.88 (d). The images were taken 20 μm into the sample and represent a sample area of about 100 $\mu\text{m}\times 80$ μm. In all cases the direction of the oscillatory shear is left-right as indicated by the arrow.

III. RESULTS AND DISCUSSION

Conventional microscopy and light scattering echo were done with sample A, while confocal microscopy was used with sample B, the latter containing larger particles (Sec. II A). We describe the conventional microscopy and light scattering echo experiments with sample A first (Sec. III A) followed by the confocal microscopy experiments with sample B (Sec. III B).

A. Conventional microscopy and light scattering echo

Figure 2(a) shows a typical DIC image of a gel before shearing. This particular image was taken about 20 μm below the top plate of the shear cell. There are several voids with sizes ranging from a few to ten particle diameters. No crystalline order can be discerned. During observations, we saw little or no particle motion at this or any other depths, and there were no observable changes within a period of about an hour. In contrast, within a distance of up to about 10 μm from the shear plates the gel structure was often densified. All images were obtained deep enough into the sample to avoid these wall effects. We have studied the effect of oscillatory shear at shear frequencies $f=70$ Hz, 10 Hz, and 1 Hz and with different strain amplitudes γ_0.

We first discuss our experiments at 70 Hz. The strain amplitude γ_0 was increased in steps. Each amplitude was applied for typically 2 min and then stopped for microscopy, which took several minutes. In all cases, the structure appeared frozen as soon as the shear was stopped. At $\gamma_0 \lesssim 0.1$, the structure appeared statistically identical to that of the quiescent ($\gamma_0=0$) gel. Increase of γ_0 beyond this value led to partial crystallization of the sample. Figure 2(b) shows a typical image after shearing at $\gamma_0=0.13$ for a few minutes. Small regions of order can be seen in an otherwise amorphous background. Scanning through the sample showed the ordered regions to be typically three dimensional. Void regions comparable in extent to the ordered patches can also be seen. In other portions of the sample, larger ordered regions and voids were observed. In all cases, the orientation of the ordered regions appeared random. Moreover, the crystalline regions did not move relative to the amorphous background over several minutes. Increasing γ_0 increased the order; Fig. 2(c) shows the gel after shearing at $\gamma_0=0.27$. Small- and medium-sized ordered domains separated by small voids or disordered regions can be seen. Now there appeared to be a common orientation to some domains that were not in contact. The large voids shown in this figure were not observed very frequently, although this may partly be due to the difficulty of observing these due to out-of-focus light from nearby particles. Increasing the strain amplitude to $\gamma_0 \gtrsim 0.4$ decreased the size and number of ordered domains. Interestingly, some very large voids were observed near the top plate of the shear cell. At the highest strain reached, $\gamma_0=0.88$, the sample became almost completely amorphous, with only very small crystalline regions remaining, Fig. 2(d).

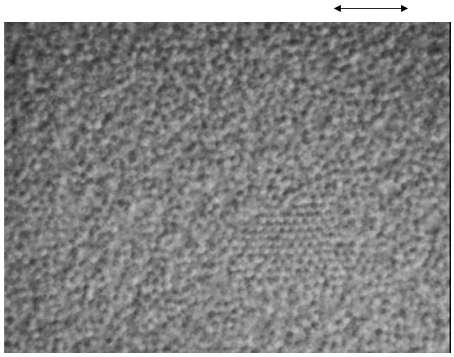

FIG. 3. Optical DIC microscopy image of a colloid-polymer gel after 2 min of oscillatory shear at a frequency $f=10$ Hz and a strain amplitude of $\gamma_0=0.24$.

Observations at 10 Hz following the same protocol showed no structural changes below $\gamma_0=0.24$. At this strain, a few ordered regions appeared, Fig. 3. Shearing at $\gamma_0=0.3$ without going through intermediate strain amplitude at this frequency gave rise to some highly ordered regions coexisting with amorphous structure, but the amount of order was less than for the same γ_0 at 70 Hz. Higher strain amplitudes at this frequency were unobtainable due to mechanical limitations of the shear cell. Finally, experiments at 1 Hz produced no crystallization at all accessible amplitudes, i.e., up to $\gamma_0=0.3$.

Our observations at all three frequencies are summarized in a shear state diagram (Fig. 4). The critical strain amplitude at which shear induced crystallization is observed clearly increases as the frequency is lowered from 70 to 10 Hz, while at the lowest frequency studied, 1 Hz, no crystallization was observed for strain amplitudes up to 0.3.

To supplement these results from conventional microscopy, we studied the same sample at 70 Hz using LS echo. Following the peaks of the echoes we essentially measure the

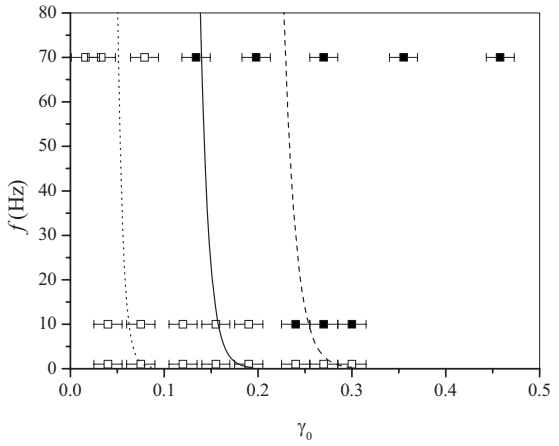

FIG. 4. State diagram of the colloid-polymer gel under oscillatory shear as a function of shear frequency f and strain amplitude γ_0. Amorphous gel samples are represented by open squares and crystalline samples by solid squares. Note that at 70 Hz and $\gamma_0=0.88$ the crystals partially melted. The predictions for the yielding/crystallization boundary are indicated by lines (see text for details of the model) and are based on $U_0=-22k_BT$ and $\tau_c=3.6$ s. The dashed line corresponds to two particles on top of each other, i.e., $z_0=2R$ [Eq. (2)] and the dotted line to the most efficient initial configuration [Eq. (4)]. The solid line depicts an average of these two lines corresponding to some intermediate particle configuration.

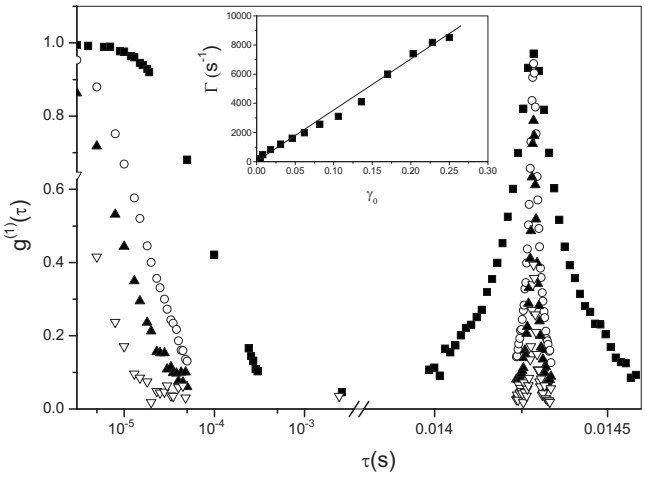

FIG. 5. Normalized field autocorrelation function $g^{(1)}(\tau)$ as obtained by dynamic light scattering echo (LS echo) during oscillatory shear at a frequency of $f=70$ Hz and for a sample thickness of $d=1.3$ mm. Shown are the initial decay and the first echo for different strain amplitudes; $\gamma_0=0.02$ (■), $\gamma_0=0.14$ (●), $\gamma_0=0.17$ (▲), $\gamma_0=0.23$ (▼). The inset shows the inverse half width at half height of the first echo, Γ, as a function of strain amplitude γ_0.

correlation function under oscillatory shear eliminating the effect of the affine oscillatory flow, thus monitoring the shear-induced dynamics in the sample. After loading the sample into the shear cell, we typically monitored $g^{(1)}(\tau)$ for half an hour to ensure that transients had died down before commencing with the shear experiments. The strain amplitude γ_0 was increased stepwise. Echo measurements at each γ_0 lasted about 15 min, so that a typical experiment took less than about 6 h. In Fig. 5 we show the normalized field autocorrelation function $g^{(1)}(\tau)$ under oscillatory shear at 70 Hz for the small delay times τ, i.e., the initial decay due to shear, and for $\tau \approx T$, i.e., delay times correlating events separated by one oscillation period, which corresponds to the first echo. With increasing strain amplitude, $g^{(1)}(\tau)$ decays faster at small τ and the echo narrows around $\tau \approx T$. The half width at half height of the first echo measures the inverse initial decay rate Γ^{-1}. For stick boundary conditions we expect $\Gamma \propto \dot{\gamma}$ [12], which, for sinusoidal strain, translates to a proportionality between the decay rate Γ and the strain amplitude γ_0. Such linearity is indeed observed (Fig. 5, inset), thus indicating the absence of wall slip in our experiments.

The height of the first echo is virtually independent of strain amplitude for $\gamma_0 \lesssim 0.15$. Above this amplitude, the echo height significantly decreases with γ_0. Figure 6 shows the same trend for the height of the first 20 echoes. It also indicates a dramatic change of the shear induced particle rearrangements between $\gamma_0=0.136$ and $\gamma_0=0.170$. At and above the latter strain amplitude, all echoes with delay time above about 1 s decay virtually completely. In other words, at 70 Hz such strain amplitudes cause irreversible rearrangements on the length scale of about $R/4$, the length scale probed in our LS echo experiments (Sec. II C), over a time scale of about 1 s. Although for small γ_0 the decay is only modest, we fit an exponential decay to all $g^{(1)}(\tau_m)$ to obtain an estimate of the characteristic relaxation time τ_{slow}. This can serve as an indication for the time scale of the slow relaxation (Fig. 7). We observe a dramatic reduction in τ_{slow} around $\gamma_0 \approx 0.15$. (Note the logarithmic scale.) These observations are entirely consistent with our conventional microscopy data at 70 Hz, which show shear-induced crystallization beginning at a strain amplitude of 0.13 (Fig. 7, open squares), while for $\gamma_0 < 0.13$ the amorphous gel remains (filled squares).

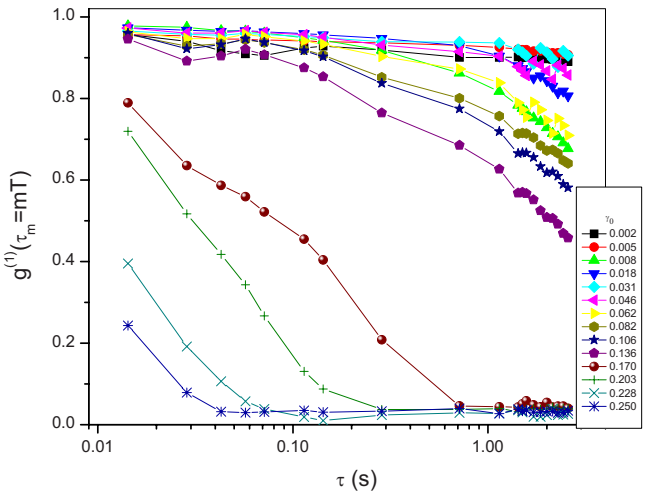

FIG. 6. (Color online) Normalized field autocorrelation function $g^{(1)}(\tau_m)$ as obtained by dynamic light scattering echo (LS echo) during oscillatory shear at a frequency of $f=70$ Hz and for a sample thickness of $d=1.3$ mm. Shown are the heights of the first 20 echoes, $g^{(1)}(\tau_m=mT)$, for different strain amplitudes γ_0 as indicated.

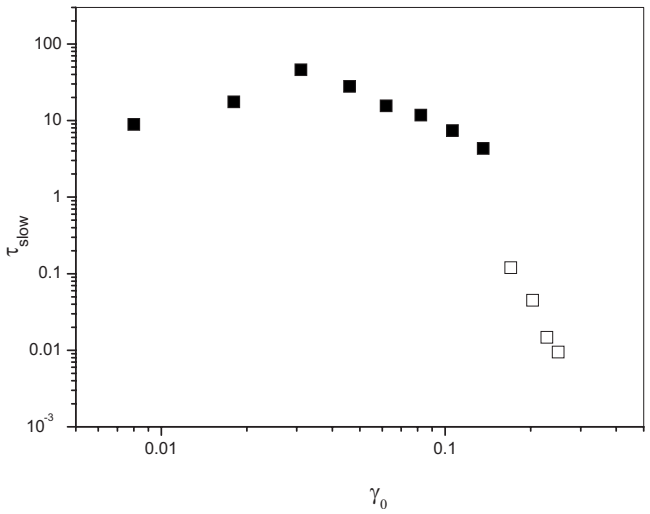

FIG. 7. Slow relaxation time τ_{slow} as a function of strain amplitude γ_0 as determined from the normalized field autocorrelation function $g^{(1)}(r)$, which was obtained by dynamic light scattering echo during oscillatory shear at a frequency of $f=70$ Hz and for a sample thickness of $d=1.3$ mm (Fig. 6). Optical microscopy allows us to distinguish amorphous gels (■) from crystalline samples (□).

B. Confocal microscopy

To obtain quantitative structural information, we performed another series of shear experiments using a confocal microscope. To enable more accurate determination of particle positions, we used sample B (Table I) in which the particles were approximately twice the size of those in sample A. The larger particle size required density matching to reduce the effect of gravity. Using the same polymer at about the same overall concentration led to about half the effective size ratio and about double the depletion potential. Moreover, the addition of CHB can lead to charge on the PMMA particles where the quantitative effects are sample dependent (see, e.g., [31]). Thus samples A and B are not directly comparable. However, we found that qualitative features observed by conventional microscopy in sample A were also observed in sample B by confocal microscopy.

Figure 8(a) shows a confocal image of sample B at rest, while Figs. 8(b)–8(d) are confocal images of the sheared samples (taken after cessation of shear); the samples were sheared for 31 min at 70 Hz with a strain amplitude $\gamma_0=0.15$. The structure shown in Fig. 8(b) is typical of the sheared sample. It is clearly different from the quiescent structure [Fig. 8(a)]; small ordered groups of particles coexist with disordered regions and small voids. Although not typical, there are also more ordered regions [Fig. 8(c)] and large voids [Fig. 8(d)] in the same sample. We also observed "Swiss cheese" crystal structures, crystalline regions separated by voids [Fig. 8(d)]. The presence of voids is unsurprising, because the crystallites are much denser (we expect $\phi \gtrsim 0.55$ [32]) than the average volume fraction in the sample ($\phi=0.44$). It is, however, astonishing that the crystalline regions are interconnected. For all sheared samples, the shear induced order is also reflected in the peaks which develop in the Fourier transforms of the confocal images

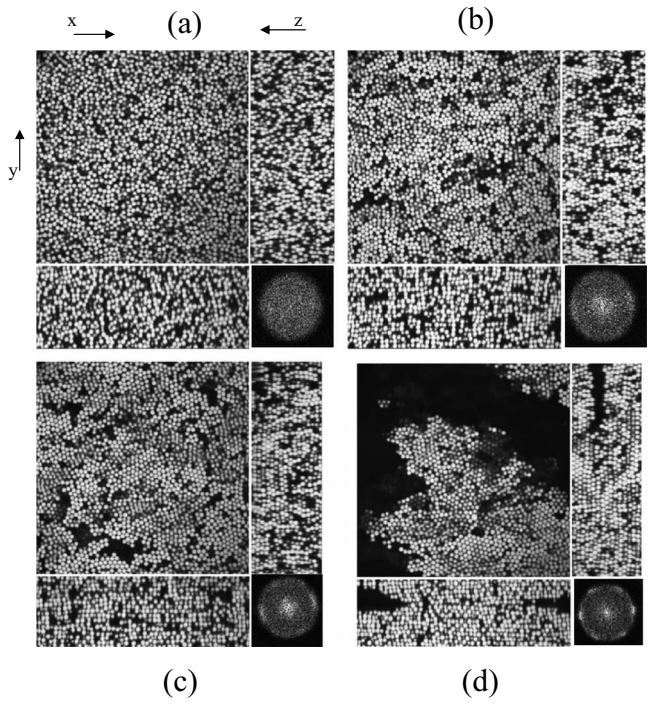

FIG. 8. Confocal microscopy results for a colloid-polymer gel in the quiescent state (a) and after 31 min of oscillatory shear at a frequency of $f=70$ Hz and a strain amplitude of $\gamma_0=0.15$ (b)–(d). The images of the sheared sample illustrate the structural diversity in the sample with a typical region (b), a highly ordered region (c) and the presence of large voids surrounded by ordered regions (d). Shown are two-dimensional slices of a three-dimensional observation volume (103 μm × 103 μm × 40 μm) in the xy plane (large square), yz plane (right), and xz plane (bottom) with the slices taken through the middle of the observation volume (axes convention as shown in Fig. 1). The fast Fourier transforms (FFT) of the xy slices are shown in the bottom right corners. For the FFT in (d) a more representative region was chosen.

(Fig. 8). Throughout the sample, all the particles were frozen in their configurations with no motion observed on our experimental time scale.

We obtained particle coordinates from the confocal images. The volume fraction in each case was calculated by counting the number of particles in a given volume. The quiescent sample gave $\phi=0.43$, while the stacks originating from sheared samples indicated $\phi=0.44$, 0.44, and 0.45, respectively. Within experimental uncertainties this is consistent with the bulk value $\phi=0.44$.

Based on the particle coordinates, we determined radial distribution functions (RDFs) in three dimensions, $g(r)$, and in the xy, xz, and yz planes, $g_{xy}(r)$, $g_{xz}(r)$, and $g_{yz}(r)$, Figure 9 (with the axes defined in Fig. 1). As expected, the quiescent sample shows little sign of order in its $g(r)$, and $g_{xy}(r)$, $g_{xz}(r)$, and $g_{yz}(r)$ appear to be identical (solid curves). Furthermore, the $g(r)$ of the sheared sample [Fig. 8(b)] shows hardly any sign of ordering. However, shear has clearly affected $g_{xy}(r)$ and $g_{xz}(r)$. The new features in $g_{xy}(r)$, especially a nearly split second peak and a broad third peak, are consistent with hexagonal close packing within this plane [Fig. 9(b), arrows indicate the peak positions expected for

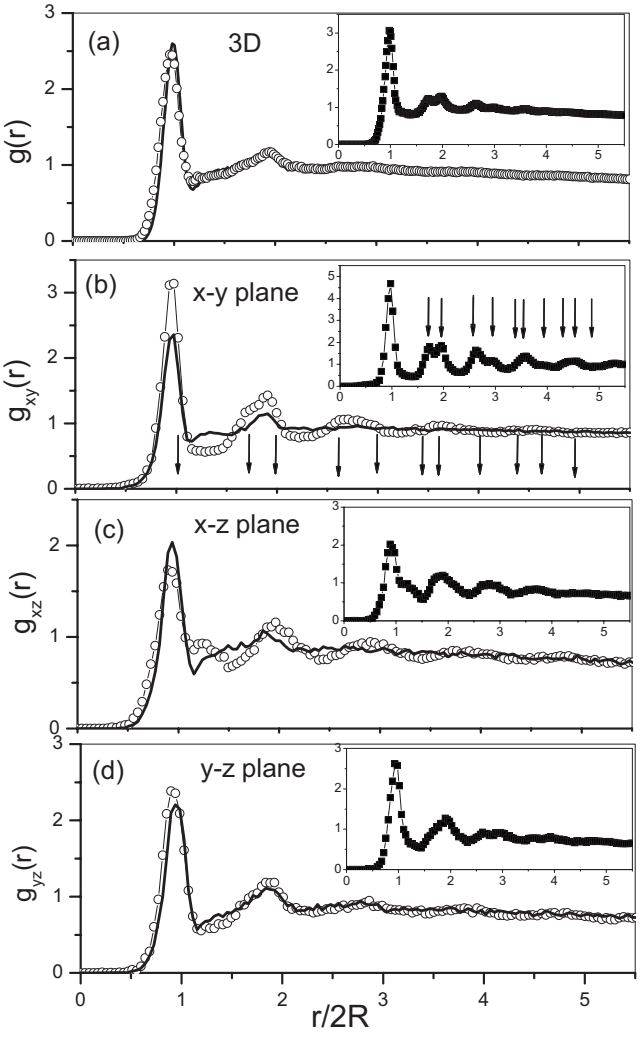

FIG. 9. Radial distribution functions (RDFs) determined from particle locations which were obtained using confocal microscopy. The RDFs were determined for three dimensions (a) and two dimensions in the xy (b), xz (c), and yz (d) planes (average of 20 planes with bin size 0.1 μm). The results for the quiescent state [corresponding to Fig. 8(a)] are represented by a solid line. A typical [Fig. 8(b)] and highly ordered [Fig. 8(d)] region of the sheared sample are represented by the open circles and filled squares (inset), respectively. The arrows in (b) indicate the peak positions expected for a two-dimensional hexagonal lattice with unit cell size $2R$. Note that the fluctuations around an almost constant value observed at large r in parts (c) and (d) give an estimate of the experimental uncertainties to be associated with the data, so that the differences between quiescent and sheared samples shown are statistically significant.

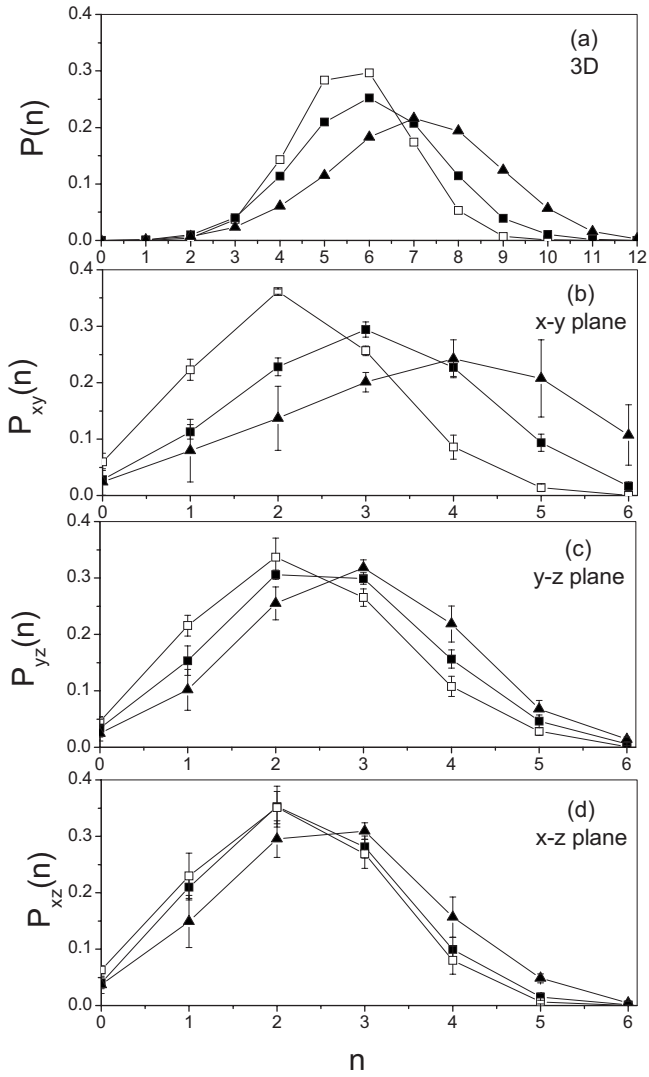

FIG. 10. Distribution $P(n)$ of the number of nearest neighbors, n, determined from particle locations which were obtained using confocal microscopy. The $P(n)$ were determined for three dimensions (a) and two dimensions in the xy (b), yz (c), and xz (d) planes. Shown are results for the quiescent state [□, corresponding to Fig. 8(a)] and a typical [■, corresponding to Fig. 8(b)] and highly ordered [▲, corresponding to Fig. 8(d)] region of the sheared sample.

hexagonal order]. These features are more pronounced for the region of high order corresponding to Fig. 8(d) (Fig. 9, insets). While there is clearly some ordering within the xz plane [Fig. 9(c)] the nature of this ordering is unclear. Perturbations to $g_{yz}(r)$ are small.

The first maximum of the radial distribution function defines the shell of nearest neighbors. We determine the distribution of the number of nearest neighbors, again in three dimensions, $P(n)$, and in the three planes, $P_{xy}(n)$, $P_{xz}(n)$, and $P_{yz}(n)$, Fig. 10. For the quiescent sample (open squares), $P(n)$ peaks at $n \approx 6$, while $P_{xy}(n)$, $P_{xz}(n)$, and $P_{yz}(n)$ all peak at $n \approx 2$ and do not show significant differences. There are no particles with six nearest neighbors in any of the three planes studied, consistent with the absence of hexagonal order. Shear induces the most significant change in $P_{xy}(n)$, Fig. 10(b) (filled squares), where we see a clear shift of the peak to higher n, consistent with a densified structure in the xy plane. More importantly, there is now a finite, but small (about 2%) fraction of particles with six neighbors. Both are consistent with the presence of hexagonal order in this plane. Again, this is more pronounced for the region of high order corresponding to Fig. 8(d) (Fig. 10, triangles).

Finally, we have computed the distribution of nearest neighbor orientations in the xy, xz, and yz planes. We calcu-

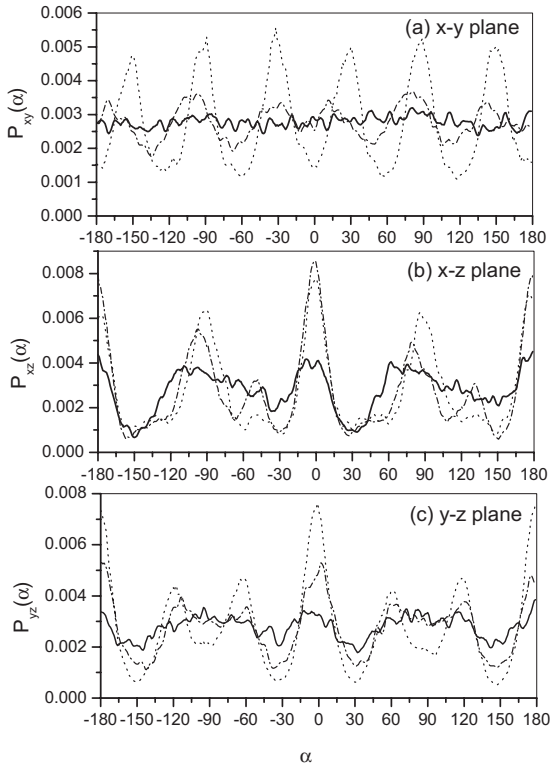

FIG. 11. Distribution $P(\alpha)$ of nearest neighbor orientations determined from particle locations which were obtained using confocal microscopy. The $P(\alpha)$ were determined in the xy (a), xz (b), and yz (c) planes with α the angle between the line connecting the particle centers and the x, x, and y axis, respectively. Shown are results for the quiescent state [solid line, corresponding to Fig. 8(a)] and a typical [dash-dotted line, corresponding to Fig. 8(b)] and highly ordered [dotted line, corresponding to Fig. 8(d)] region of the sheared sample. Note that, as expected, $P_{xy}(\alpha)$ at zero shear is essentially constant [solid line in (a)]. The fluctuations in this data set give a measure of the experimental uncertainties in all parts of this figure.

lated the orientational distributions $P_{xy}(\alpha)$, $P_{xz}(\alpha)$, and $P_{yz}(\alpha)$, Fig. 11. In each of these planes, we define α to be the angle between the vector from the particle at the origin to the center of a nearest neighbor and the x, x, and y axis, respectively. The quiescent sample [solid line, corresponding to Fig. 8(a)] has a uniform distribution of nearest neighbors within the xy plane; $P_{xy}(\alpha) \approx 0.0027 \approx 1/360$. Interestingly, however, $P_{xz}(\alpha)$ and $P_{yz}(\alpha)$ show rather more structure, to which we will return later.

Shear has a clear effect on the distribution of nearest neighbor orientations [Fig. 11, dashed-dotted and dotted line for the regions corresponding to Figs. 8(b) and 8(d), respectively]. Instead of being constant, $P_{xy}(\alpha)$ now shows distinct, quasiregular oscillations with a period of about 60° [Fig. 11(a)] indicative of a tendency toward aligned hexagonal packing. The position of these oscillations suggests a tendency for lines of closest packing to align along the vorticity direction (y axis), perpendicular to the shear direction (x axis). The same alignment occurs in shear-induced crystallites of a colloidal glass of PMMA particles ($\phi = 0.56$) under low amplitude ($\gamma_0 \lesssim 0.5$) oscillatory shear [21]. Note, however, that the rather shallow minima near 0° and ±180° in Fig. 11(a) are indicative of a significant minority alignment of closest-packing particles *along* the shear direction (x axis).

The predominant alignment of lines of closest-packing particles in the xy plane along the y axis shows up as prominent peaks at 0° and ±180° in $P_{yz}(\alpha)$, Fig. 11(c). The other peaks of $P_{yz}(\alpha)$ at about ±60° and about ±120° suggest that there is a (perhaps surprising) tendency toward hexagonal ordering in this plane. On the other hand, the very shallow minima at about ±90° suggest that many particles are stacked directly above each other in the z direction. The yz slice in Fig. 8(b) does indeed show regions of hexagonal order and of lines of particles in the z direction. The z stacking of particles is very prominent in the xz slice shown in Fig. 8(b), and shows up as prominent peaks at about ±90° in $P_{xz}(\alpha)$, Fig. 11(b). The small peaks at around −60° and around 120° are consistent with the presence of hexagonal packing in the yz plane evidenced by $P_{yz}(\alpha)$.

We now return to the nonflatness of $P_{xz}(\alpha)$ and $P_{yz}(\alpha)$ for the unsheared sample. It is conceivable that the excess of particles at 0° and ±180° may be an artifact due to the elongation of the point spread function (the image of an ideal point source) along the z (or optic) axis. On the other hand, comparing $P_{xz}(\alpha)$ and $P_{yz}(\alpha)$ for the unsheared and sheared samples, we see that plausibly, the weak features in the former sharpen into the prominent features in the latter. This suggest that even the flow associated with loading the sample into the shear cell induces weak ordering in the xz and yz planes, but without inducing crystallization in the xy plane. In particular, the broad "plateaus" centered around ±90° in $P_{xz}(\alpha)$ and $P_{yz}(\alpha)$ for the unsheared sample (or, equivalently, the minima at ±30° and ±150°) suggest the beginning of particles stacking in the z direction. It is intuitively obvious that such stacking facilities flow parallel to the xy plane.

IV. SHEAR MODEL

We present a heuristic model which aims at understanding the location of the yielding/crystallization boundary in the shear state diagram (Fig. 4). The essential idea is this: Shear strain pulls each particle away from its neighbor, i.e., the minimum of the attractive potential well. As it does so, the probability for escape from the interparticle attraction increases. The "attempt frequency" for such escape is proportional to the frequency of the applied shear, which dominates diffusion under the conditions of our experiments. We postulate that when the characteristic escape time becomes shorter than a critical time scale τ_c the particles become essentially "free" and can rearrange to form crystallites.

Consider first the case of two attractive particles sitting directly on top of each other along the gradient direction (z axis). Shearing in the x direction (Fig. 1) will separate the particles. If we model the depletion attraction by a linear ramp with depth $U_0 = U_{\mathrm{dep}}$ and range $2\xi^* R$, then the interaction between these two particles at a shear strain of γ_0 is

$$U(\gamma_0, \xi^*) = U_0\left(1 - \frac{\gamma_0^2}{2\xi^*}\right). \quad (1)$$

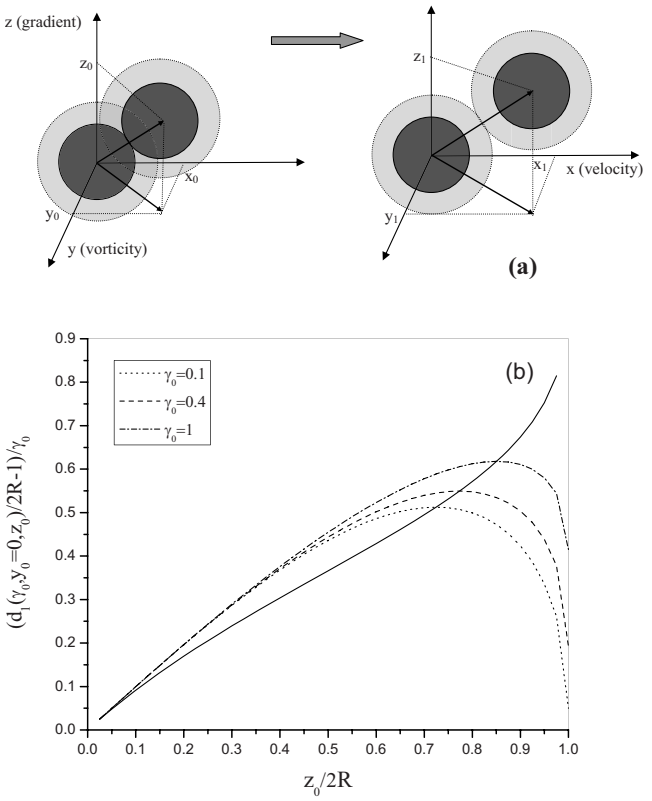

FIG. 12. (a) Schematic drawing illustrating the effect of shear on the particle distance. One particle is held fixed at the origin, while the second moves from (x_0,y_0,z_0), i.e., contact, to (x_1,y_1,z_1), where their depletion layers (light gray region) which corresponds to the range of their attractive interactions, cease to overlap. (b) Effect of the initial position $z_0/2R$ on the normalized distance that the particles are pulled apart, $[d_1(\gamma_0,y_0,z_0)/2R-1]/\gamma_0$, for different shear strain amplitudes γ_0 as indicated $(y_0=0)$. The solid line denotes the maximum normalized distance reached at different γ_0.

When γ_0 reaches a critical value, $\gamma_0^{\max}$, the nearest surface-to-surface separation will become equal to the range of the interparticle attraction, $2\xi^* R$ in our system. At even higher strain amplitudes, the particles will no longer interact: $U(\gamma_0 \geq \gamma_0^{\max})=0$. For $\xi^* \ll 1$, geometry gives

$$\gamma_0^{\max} = \sqrt{(\xi^*)^2 + 2\xi^*} \simeq \sqrt{2\xi^*}. \tag{2}$$

For our system, $\xi^*=0.05$, so that $\gamma_0^{\max} \simeq 0.32$. This is double the strain amplitude beyond which we observed yielding/crystallization (about 0.15). Nevertheless, this simple calculation suggests that shear-induced escape of particles from their mutual attractive potential wells may be the physical basis of our observations.

The geometry considered so far is not the most efficient way for shear to separate two particles. Consider a pair of touching particles (both with radius R) with one at the origin and the position of the second characterized by its initial coordinates $(x_0=(4R^2-y_0^2-z_0^2)^{1/2}, y_0, z_0)$ [Fig. 12(a)]. After a shear strain of amplitude γ_0 in the x direction the second particle moved to $(x_1=x_0+\gamma_0 z_0,\ y_1=y_0,\ z_1=z_0)$, while the first stays at the origin. We now calculate the distance $d_1(\gamma_0,y_0,z_0)$ between the centers of the two particles after a strain amplitude γ_0 has been applied. The distance $d_1(\gamma_0,y_0,z_0)$ depends on the initial configuration. Figure 12(b) shows the dependence of $d_1(\gamma_0,y_0,z_0)$ on z_0 for fixed $y_0=0$ and γ_0. For a given γ_0, the maximum of $d_1(\gamma_0,y_0,z_0)$ with respect to y_0 and z_0 is reached if $x_0^2=2R^2(1-\gamma_0/\sqrt{\gamma_0^2+4})$, $y_0^2=0$, and $z_0^2=2R^2(1+\gamma_0/\sqrt{\gamma_0^2+4})$. This maximum, $d_1^{\max}(\gamma_0)$, is given by

$$d_1^{\max}(\gamma_0) = \left[4R^2 + 4\gamma_0 R^2 \left(1 - \frac{\gamma_0^2}{\gamma_0^2+4} \right)^{1/2} + 2\gamma_0^2 R^2 \left(1 + \frac{\gamma_0}{\sqrt{\gamma_0^2+4}} \right) \right]^{1/2}.$$

The strength of the depletion potential at $d_1^{\max}(\gamma_0)$ is then

$$U'(\gamma_0,\xi^*) = U_0 \left(1 - \frac{d_1^{\max}(\gamma_0) - 2R}{2\xi^* R} \right). \tag{3}$$

The factor in brackets represents the largest factor by which shear of amplitude γ_0 can reduce the attractive interaction between a pair of initially touching particles.

Using the Kramers approach, we estimate the escape time of particles confined to potential wells [33]. The Kramers escape time for a Brownian particle confined by a potential of the Asakura-Oosawa form can be calculated numerically [34]. However, to obtain analytic results, we have to approximate this potential. The simplest approximation is a square well of depth $U=U_{\text{dep}}$ and width $\delta^*=2\xi^* R$, for which the escape time is

$$\tau_{\text{escape}} = \frac{\delta^{*2}}{D_s} e^{-\beta U}, \tag{4}$$

where $\beta=1/k_B T$ and D_s is the (self-)diffusion coefficient of the particle inside the well. The inverse of the prefactor, $(\delta^{*2}/D_s)^{-1}$, can be seen as an "attempt frequency."

A better approximation is a ramp potential of the same depth and width. The escape time is now [34]

$$\tau_{\text{escape}} = \frac{1}{D_s} \int_0^{\delta^*} dx' e^{\beta U(x')} \int_{-\infty}^{x'} dx e^{-\beta U(x)} = \frac{\delta^{*2}}{D_s} \frac{e^{-\beta U} - (1-\beta U)}{(\beta U)^2}. \tag{5}$$

The escape time from a ramp potential is smaller than from a square well potential, because the ramp potential is shallower than a square well potential (except at contact). Extending this argument, we expect that for an Asakura-Oosawa potential of the same range and depth at contact, the particles should be able to escape more easily and thus τ_{escape} should be lower because the ramp potential overestimates the strength of the attraction (again, except at contact).

The escape time τ_{escape} sets the time scale for particle rearrangements involving "bond breaking" in the quiescent gel. To estimate τ_{escape} we require the diffusion coefficient D_s for particles confined to each others' potential wells. An

estimate for this can be obtained by assuming that the local volume fraction in the gel is that of a suspension in which the average surface-to-surface separation is twice the thickness of the depletion zone; this yields a volume fraction $\phi_{\text{local}} \approx 0.55$. The short-time self-diffusion coefficient of a particle in a hard-sphere suspension with $\phi \approx 0.55$ is 20% of the free-particle value [36], giving $D_s = 2 \times 10^{-10}$ cm^2 s^{-1}. Using $\delta^* = 2\xi^* R = 72$ nm and $\beta U = \beta U_{\text{dep}} = -22$ (Table I) we obtain $\tau_{\text{escape}} \approx 22$ days. This is consistent with the fact that we observed very little or no particle motion in the quiescent gel.

Now consider two particles under oscillatory shear. Shear moves the particle closer to the edge of its neighbor's attractive potential. Thus the particle has to escape from a reduced potential, which depends on the particles' relative initial position, but is at least $U'(\gamma_0, \xi^*)$. The particles reach their maximum separation where the probability for escape is highest twice per cycle. We hence estimate the attempt frequency by twice the shear frequency, $2f = 2/T$. This attempt frequency $2f$ (140 and 20 s^{-1}, respectively) is larger than the thermal attempt frequency $D_s/\delta^{*2} \approx 3.8$ s^{-1}. Together with the shear-induced reduction of the attractive potential well, the escape is thus expected to be controlled by shear and the thermal contribution can be neglected. The shear-induced Kramers escape time becomes

$$\tau_{\text{escape}} = \frac{1}{2f} \frac{e^{-\beta U} - (1 - \beta U)}{(\beta U)^2}. \tag{6}$$

For U we may use either Eqs. (1) or (3).

If we assume that rearrangements leading to crystallization take place when τ_{escape} drops below a characteristic time τ_c, then the yielding/crystallization boundary in the shear state diagram should be given by

$$f(\gamma_0) = \frac{1}{2\tau_c} \frac{e^{-\beta U(\gamma_0)} - [1 - \beta U(\gamma_0)]}{[\beta U(\gamma_0)]^2}. \tag{7}$$

We now require an estimate for τ_c. In our colloid-polymer mixture at zero shear the arrest into a gel state occurs when the contact value of the depletion potential is about $\beta U_{\text{dep}} \approx -2.7$ [35]. At slightly lower depth of the potential, the sample crystallizes. Thus the rearrangement time under these conditions is the largest possible τ_{escape} for crystallization to occur. To estimate τ_{escape} for a sample at the gelation boundary, we proceed as above when estimating τ_{escape} for the quiescent gel. Using $\beta U_{\text{dep}} \approx -2.7$, $D_s = 2 \times 10^{-10}$ cm^2 s^{-1}, and $\delta = 2\xi R = 2r_g = 216$ nm (since the gelation boundary is located at $c_p < c^*$) we obtain $\tau_c \approx 3.6$ s. This value is consistent with our LS echo results (Fig. 7); $\tau_c = 3.6$ s is indeed situated in the transition region of the slow relaxation time, τ_{slow}, from noncrystallizing to crystallizing behavior.

Using $\tau_c = 3.6$ s in Eq. (7), we can estimate the frequency $f(\gamma_0)$ required for yielding/crystallization at a given strain amplitude γ_0, which enters via the potential $U(\gamma_0, \xi^*)$ given either by Eqs. (1) or (3). Figure 4 compares the observed the f vs γ_0 state diagram with the yielding/crystallization boundary predicted for two initial particle configurations; two particles initially sitting on top of each other [Eq. (1)] and in the most efficient initial configuration [Eq. (3)]. The actual sample will contain particles in these and many other configurations. Nevertheless, given the simplicity of the model, these two configurations bracket the observed boundary reasonably well. Moreover, it is interesting, that the *average* between the predicted crystallization boundaries for these two initial configurations (continuous line in Fig. 4) corresponds reasonably well with the observed boundary.

Our samples are inherently many-body systems. In contrast, our model considers only a single particle-particle "bond" between two particles at a time. It implicitly assumes that it is crucial to break the bond to the nearest neighbor in the neighboring xy plane (i.e., shear plane, Fig. 12). The existence of xy planes of particles, at least on a local scale, is supported by confocal microscopy (Fig. 8) and, in a more quantitative way, by the peaks at 0° and 180° in $P_{xz}(\alpha)$ and $P_{yz}(\alpha)$ [Figs. 11(b) and 11(c)]. Furthermore, there are typically two bonds connecting a particle to particles in the neighboring xy planes [Figs. 10(c) and 10(d)], i.e., there is typically one bond from one particle to a particle in a neighboring xy plane. Breaking the bond between particles in neighboring xy planes depins them from each other. Successive rearrangements within the xy planes and even "rolling" into a neighboring xy plane do not necessarily involve further bond breaking. (The possibility of bond formation, i.e., that a particle gets trapped in another potential, before it finds its place in a crystalline structure, is neglected.) Local hexagonal ordering in two dimensions is known to be rapid. This might explain why, despite a number of simplifications, our single-bond–two-particle model seems to capture the essential physics.

V. CONCLUSIONS

Our main findings are summarized in Fig. 4. Conventional and confocal microscopy as well as dynamic light scattering echo experiments showed that colloid-polymer gels can crystallize under oscillatory shear with modest shear strain amplitudes γ_0, while high γ_0 melt the crystals again. The shear strain amplitude required for irreversible particle rearrangements or yielding seems to coincide with that required for crystallization. It decreases as the oscillation frequency increases. We presented a simple model which can reproduce these observations semiquantitatively. It is based on the shear-assisted escape of a particle from the attractive potential of its neighbor. When the characteristic escape time becomes shorter than a critical time scale τ_c, the particles can rearrange to form crystallites.

Recently confocal microscopy has been applied to elucidate the microstructure of colloid-polymer gels at volume fractions lower than studied here; $\phi \lesssim 0.4$ [31,37]. We are now extending our investigations to shear-induced crystallization in such dilute gels. As the colloid volume fraction decreases, the particles are expected to organize less in xy planes, but the assumption that a particle, after a shear-induced escape, is not captured by another particle should become increasingly valid. It is thus interesting to test the applicability (or otherwise) of our simple shear model under these conditions.

Finally, we comment on our findings in the light of recent work on the yielding of colloidal glasses and gels [22]. Oscillatory bulk rheology showed that a hard-sphere (or repulsion-dominated) glass at $\phi \approx 0.6$ under oscillatory shear yielded in a single step via "cage breaking," while an attractive glass at the same ϕ yielded in two steps, successively breaking interparticle bonds and then cages. Interestingly, a $\phi \approx 0.4$ attractive gel similar to the one studied here does not show a clear two step yielding. The results reported above support this finding: we observed a single onset of irreversible rearrangements, coincident with crystallization. In future work, it would be interesting to study the yielding and shear-induced crystallization of a high-volume-fraction attractive colloidal *glass* using LS echo. The findings in [22] suggest that, in this case, we may observe some irreversible rearrangement commencing at low strain amplitude associated with bond breaking, and then the onset of a second stage of irreversible rearrangements when cages break at higher strain amplitude, the latter presumably coincident with the onset of crystallization.

ACKNOWLEDGMENTS

We thank Andrew Schofield for the synthesis of the PMMA particles and Peter Pusey and Peter Olmsted for valuable discussions. P.S. was funded by the UK Engineering & Physical Sciences Research Council. G.P. acknowledges funding by the EU Marie Curie ToK "COSINES" and S.U.E. by the Deutsche Forschungsgemeinschaft (Collaborative Research Center SFB-TR6, Project Section A6). The Edinburgh-Crete collaboration during the final stages of this work was partly funded by the EU Network of Excellence "SoftComp."

[1] A. M. Alsayed, M. F. Islam, J. Zhang, P. J. Collings, and A. G. Yodh, Science **309**, 1207 (2005).
[2] K. N. Pham *et al.*, Science **296**, 104 (2002).
[3] V. Prasad, D. Semwogerere, and E. R. Weeks, J. Phys.: Condens. Matter **19**, 113102 (2007).
[4] I. Cohen, T. G. Mason, and D. A. Weitz, Phys. Rev. Lett. **93**, 046001 (2004).
[5] D. Derks, H. Wisman, A. van Blaarderen, and A. Imhof, J. Phys.: Condens. Matter **16**, S3917 (2004).
[6] T. C. B. McLeish and S. T. Milner, Adv. Polym. Sci. **143**, 195 (1999).
[7] M. E. Cates, Ann. Henri Poincare **2** (*Suppl.*), S647 (2003).
[8] M. Fuchs and M. E. Cates, Phys. Rev. Lett. **89**, 248304 (2002).
[9] J. M. Brader, T. Voigtmann, M. E. Cates, and M. Fuchs, Phys. Rev. Lett. **98**, 058301 (2007).
[10] V. Kobelev and K. S. Schweizer, Phys. Rev. E **71**, 021401 (2005).
[11] G. Petekidis, P. N. Pusey, A. Moussaid, S. Egelhaaf, and W. C. K. Poon, Physica A **306**, 334 (2002).
[12] G. Petekidis, A. Moussaid, and P. N. Pusey, Phys. Rev. E **66**, 051402 (2002).
[13] P. Hébraud, F. Lequeux, J. P. Munch, and D. J. Pine, Phys. Rev. Lett. **78**, 4657 (1997).
[14] S. Asakura and F. Oosawa, J. Polym. Sci. B **22**, 1255 (1954).
[15] W. C. K. Poon, J. Phys.: Condens. Matter **14**, R859 (2002).
[16] L. Starrs, W. C. K. Poon, D. J. Hibberd, and M. M. Robins, J. Phys.: Condens. Matter **14**, 2485 (2002).
[17] W. C. K. Poon, L. Starrs, S. P. Meeker, A. Moussaid, R. M. L. Evans, P. N. Pusey, and M. M. Robins, Faraday Discuss. **112**, 143 (1999).
[18] H. N. W. Lekkerkerker, W. C. K. Poon, P. N. Pusey, A. Stroobants, and P. B. Warren, Europhys. Lett. **20**, 559 (1992).
[19] E. J. Meijer and D. Frenkel, J. Chem. Phys. **100**, 6873 (1994).
[20] D. G. A. L. Aarts, R. Tuinier, and H. N. W. Lekkerkerker, J. Phys.: Condens. Matter **14**, 7551 (2002).
[21] M. D. Haw, W. C. K. Poon, and P. N. Pusey, Phys. Rev. E **57**, 6859 (1998) Note that *peak-to-peak* strain amplitudes were reported in this paper. These values should be halved when comparing with γ_0 in the present work.
[22] K. N. Pham, G. Petekidis, D. Vlassopoulos, S. U. Egelhaaf, P. N. Pusey, and W. C. K. Poon, Europhys. Lett. **75**, 624 (2006).
[23] V. Martellozo, Ph.D. thesis, The University of Edinburgh, Edinburgh, 2001.
[24] G. C. Berry, J. Chem. Phys. **44**, 4550 (1966).
[25] V. Prasad, Ph.D. thesis, Harvard University, Boston, 2002.
[26] P. A. Smith, Ph.D. thesis, The University of Edinburgh, Edinburgh, 2004.
[27] M. S. Elliot and W. C. K. Poon, Adv. Colloid Interface Sci. **92**, 133 (2001).
[28] J. C. Crocker and D. G. Grier, J. Colloid Interface Sci. **179**, 298 (1996).
[29] R. Höhler, S. Cohen-Addad, and H. Hoballah, Phys. Rev. Lett. **79**, 1154 (1997).
[30] C. M. Sorensen, R. C. Mockler, and W. J. O'Sullivan, Phys. Rev. A **14**, 1520 (1976).
[31] A. I. Campbell, V. J. Anderson, J. S. van Duijneveldt, and P. Bartlett, Phys. Rev. Lett. **94**, 208301 (2005).
[32] S. M. Ilett, A. Orrock, W. C. K. Poon, and P. N. Pusey, Phys. Rev. E **51**, 1344 (1995).
[33] H. A. Kramers, Physica A **7**, 284 (1940).
[34] T. McLeish, in *Soft and Fragile Matter, Non Equilibrium Dynamics, Metastability and Flow*, edited by M. E. Cates and M. R. Evans (Institute of Physics, Bristol, 2000).
[35] J. Bergenholtz, W. C. K. Poon, and M. Fuchs, Langmuir **19**, 4493 (2003).
[36] P. N. Segre, O. P. Behrend, and P. N. Pusey, Phys. Rev. E **52**, 5070 (1995).
[37] C. J. Dibble, M. Kogan, and M. J. Solomon, Phys. Rev. E **74**, 041403 (2006).